PHYSICAL REVIEW B **88**, 024406 (2013)

Thermally induced dynamics in ultrathin magnetic tunnel junctions

P. Ogrodnik
Warsaw University of Technology, Faculty of Physics, Koszykowa 75, 00-662 Warszawa, Poland and Institute of Molecular Physics, Polish Academy of Sciences, Smoluchowskiego 17, 60-179 Poznań, Poland

G. E. W. Bauer
Institute for Materials Research and WPI-AIMR, Tohoku University, Sendai 980-8577, Japan and Kavli Institute of NanoScience, Delft University of Technology, NL-2628 CJ Delft, the Netherlands

Ke Xia
Department of Physics, Beijing Normal University, Beijing 100875, China

(Received 30 September 2012; revised manuscript received 13 April 2013; published 8 July 2013)

We consider the magnetization dynamics induced by thermally induced spin transfer torques in thin Fe|MgO|Fe tunnel junctions. The magnetization dynamics is described by the Landau-Lifshitz-Gilbert equation, including the thermal torques as computed from first principles. We show that the angular skewness of the torques importantly modifies the dynamics, e.g., leading to different instability criteria.

DOI: 10.1103/PhysRevB.88.024406 PACS number(s): 75.78.Jp, 85.75.Dd, 72.25.Ba, 05.45.−a

I. INTRODUCTION

One of the challenges for spin electronics is to find easy and efficient methods to manipulate the magnetic order parameter. For this reason, the current-induced spin transfer torque (STT) has attracted a lot of attention by scientists and engineers, since it promises control of magnetism by a voltage bias without the need for external magnetic fields.[1–3] This STT has been observed in metallic multilayer pillars (spin valves) and magnetic tunnel junctions (MTJs). The STT effect is caused by spin-polarized electrons that change their angular and magnetic momentum direction by flowing through noncollinearly magnetized layers. At sufficiently high current densities, the torque felt by the magnetization can overcome the magnetic damping and lead to precession and ultimately switching. The STT on a magnetization consists of two components. One is spanned by the magnetization and spin-current polarization (in plane), while a second one is normal to this plane (also called the effective field). In contrast to metallic spin valves,[4] both components can be of similar magnitude in MTJs.[5–8]

In practice, the STT is employed in spin valves and MTJs in which one layer is much thinner than the other (the so-called free layer) such that magnetization dynamics are easily induced. The other layer acts as polarizer for the electric current, with magnetic moment pinned to one direction. In such devices, the free layer can switch to a dynamical state at certain critical system parameters. Among them we find steady-state in-plane and out-of-plane oscillations of the magnetization, switching between antiparallel (AP) and parallel (P) configurations, static canted states, or even chaotic motion.[9,10]

In symmetric MTJs with very thin tunneling barriers of typically MgO, in which both magnetic layers consist of the same material, e.g., in-plane magnetized CoFeB, large-amplitude out-of-plane oscillations can be induced without an external magnetic field.[11] However, thicker MTJs with interfacial perpendicular anisotropy may exhibit large-amplitude oscillations as well.[12] A similar effect has been observed in single asymmetric (two electrodes are made of different materials) in-plane magnetized[13,14] and double in-plane but noncollinearly magnetized metallic spin valves.[15] Out-of-plane oscillations occur also in specially designed symmetric spin valves with two strongly coupled free layers,[16] asymmetric single spin valves with interfacial perpendicular anisotropy,[17] or standard symmetric and in-plane magnetized valves, although then magnetic fields have to be applied.[18] The origin of these oscillations differs. In MTJs, a major role is played by the out-of-plane effective magnetic field that is electrically induced by the tunneling through the MgO barrier.

Spin-transfer torques in MTJs, as well as in metallic spin valves, can also be generated thermally.[19] Slonczewski[20] suggested using magnetic insulators for the polarizer that generates a thermal spin current under a temperature gradient by the spin Seebeck effect,[21] which then transfers spin momentum into the thin free magnetic layer in a spin valve with possibly very high efficiency. Heat currents across standard MTJs also generate STTs.[22] Temperature gradients in MTJs have recently been generated electrically and optically. In Ref. 23, a special heater line was employed to ensure a relatively small but steady-state temperature gradient. Alternatively, femtosecond laser pulses induce a time-dependent temperature gradient.[24,25] Their magnitude may be much larger (according to simulations, up to $\Delta T \approx 20\,\mathrm{K}$ can be achieved[25]) than for the steady-state heating, but their duration is rather short (on the order of picoseconds). *Ab initio* calculations show that the magnitude of the thermal STT may be comparable to that induced by an electric bias. However, the angular dependence in thin layers may be skewed due to multiple scattering involving interface states.[22] In heat-assisted magnetization reversal, the next step in magnetic disk data storage technology,[26] large heat currents are generated that might affect the switching characteristic of a multilayered magnetic bit. Vice versa, it could be interesting to use these heat currents to write information at small applied magnetic fields or reduced heating. In both cases, it is important to understand and model in detail the effects of thermal STTs.

In this paper, we focus on the effect of thermally induced STTs on the magnetization dynamics of MTJs, with emphasis on the critical temperature needed to switch to a dynamical state. We compare the skewed thermal torques corresponding to MTJs with ultrathin MgO barriers with thicker junctions, in which the torques are simple trigonometric functions of the relative magnetization angles. We assume here that the thermal STT is constant in time and thus do not address the dynamics induced by femtosecond laser pulses.[24] The stationary limit allows us to determine stability conditions by standard linearization of the system around equilibrium points.

The paper is organized as follows. In Sec. II, our model for the magnetization dynamics in MTJs is described. Section III summarizes the input from *ab initio* calculations of thermal torques. The method for obtaining stability criteria can be found in Sec. IV. In Sec. V, the numerical results, as well as the method of their analysis, are described. In this section, the magnetic parameters of the free layer play a role as well. The final summary and conclusions are given in the Sec. VI.

II. SPIN DYNAMICS MODEL

Figure 1 shows our model junction. It consists of two ferromagnetic iron electrodes separated by a crystalline MgO tunnel barrier.

The dynamics of the magnetization of the free layer $\vec{S}_R$ are described by the Landau-Lifshitz-Gilbert (LLG) equation

$$\frac{d\vec{S}_R}{d\tau} + \alpha \vec{S}_R \times \frac{d\vec{S}_R}{d\tau} = \vec{\Gamma}_a + \vec{\Gamma}_T \tag{1}$$

where $\vec{\Gamma}_a$ and $\vec{\Gamma}_T$ on the right-hand side are the torques exerted on magnetizations of the free layer and α is the Gilbert damping constant. $\vec{\Gamma}_a$ originates from the uniaxial and planar anisotropies, while $\vec{\Gamma}_T$ is the heat flow-related torque. The latter can be decomposed of an in-plane and out-of-plane contribution $\vec{\Gamma}_T = \vec{\tau}_\parallel + \vec{\tau}_\perp = \tau_\parallel(\vec{S}_R \times \vec{S}_L) + \tau_\perp \vec{S}_R \times (\vec{S}_R \times \vec{S}_L)$. The above equation can be expressed in spherical coordinates in dimensionless form.[27] We then obtain two differential equations for the polar θ and azimuthal ϕ angles:

$$\begin{aligned} \frac{d\theta}{d\tau} &= -\alpha \sin\theta \cos\theta - h_P \cos\phi \sin\theta \\ &\quad \times (\alpha \cos\theta \cos\phi + \sin\phi) - \mathrm{h}_\parallel \sin\theta + \alpha h_\perp \sin\theta \\ \frac{d\phi}{d\tau} &= -\cos\theta + h_P \cos\phi(\alpha \sin\phi - \cos\theta\cos\phi) \\ &\quad + \alpha \mathrm{h}_\parallel + \mathrm{h}_\perp . \end{aligned} \tag{2}$$

where $\tau = \frac{t\Omega_k}{1+\alpha^2}$ is the dimensionless time, $\Omega_K = \gamma H_K$ is the ferromagnetic resonance frequency, and H_K the uniaxial anisotropy field. Apart from the dimensionless planar anisotropy field $h_P = K_P/K$ (planar anisotropy constant K_P normalized by uniaxial anisotropy constant K), the two normalized components of thermal torques are also present in Eq. (2), i.e., in-plane torque $h_\parallel = \tau_\parallel/2Kd_f$ and out-of-plane torque $h_\perp = \tau_\perp/2Kd_f$, where d_f is the thickness of the free layer. We parameterize the angle dependence of the torques by the parameters $\Lambda_\parallel$ and $\Lambda_\perp$ that measure the deviations from the sine dependencies of the thermal torques[28] as

$$\frac{\tau_{\parallel(\perp)}}{\tau^{(0)}_{\parallel(\perp)}} = \left(\Lambda_{\parallel(\perp)} \cos^2\frac{\theta}{2} + \frac{1}{\Lambda_{\parallel(\perp)}} \sin^2\frac{\theta}{2}\right)^{-1}, \tag{3}$$

which reduces to the trigonometric dependence when $\Lambda_{\parallel(\perp)} = 1$. In that limit, the torque moduli are symmetric around $\theta = \pi/2$ but skewed when $\Lambda_{\parallel(\perp)} \neq 1$. In the next section, we discuss these parameters in more detail.

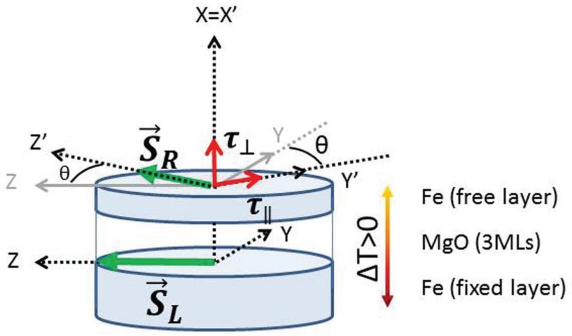

FIG. 1. (Color online) Schematic model junction examined in this paper. Green arrows indicate two magnetization vectors in the fixed (L) and free (R) layers. Local coordinates in the free layer are rotated by the angle θ with respect to that of the fixed layer. A positive temperature gradient means that left electrode is hotter than the right one.

MTJs with very thin barriers may exhibit enhanced Gilbert damping α due to spin pumping.[29] Based on the literature,[29–32] we estimated the enhancement of damping in the free layer to be $\Delta\alpha \approx 3 \times 10^{-3}$, in accordance with preliminary electronic structure calculations in which one of the layers is a normal metal. We therefore disregard spin-pumping-related effects in the following.

III. THERMAL TORQUES

As mentioned in previous sections, we focus here on the possibility of manipulating the magnetization in MTJs by heat currents induced by temperature gradients applied across the junction. The thermal torques can be computed by first principles using the Landauer-Büttiker formalism. The relevant calculations have been carried out by Jia *et al.*[22] The authors' approach assumes that the ferromagnetic layers in the MTJ system is divided onto atomic monolayers. Next, the transmission vector of the spin flowing between ith and $(i+1)$th in both directions $\vec{t}^{\,L}_{i+1,i}$, and vice versa in $\vec{t}^{\,R}_{i,i+1}$, is calculated. Having the transmission coefficients, the expression for the spin heat current between two layers can be written as

$$\vec{J}_{i+1,i} = \frac{\Delta T}{16\pi T_0} \int d\epsilon(\epsilon - \epsilon_F) \cdot \frac{\partial f}{d\epsilon}\left(\vec{t}^{\,L}_{i+1,i}(\epsilon) + \vec{t}^{\,R}_{i,i+1}(\epsilon)\right) \tag{4}$$

where $\Delta T = T_L - T_R$ denotes the global temperature difference, f is the Fermi-Dirac distribution, and the mean temperature of the junction is $T_0 \equiv (T_L + T_R)/2$. The above expression includes only the spin current induced by the temperature gradient. We omit here the equilibrium spin

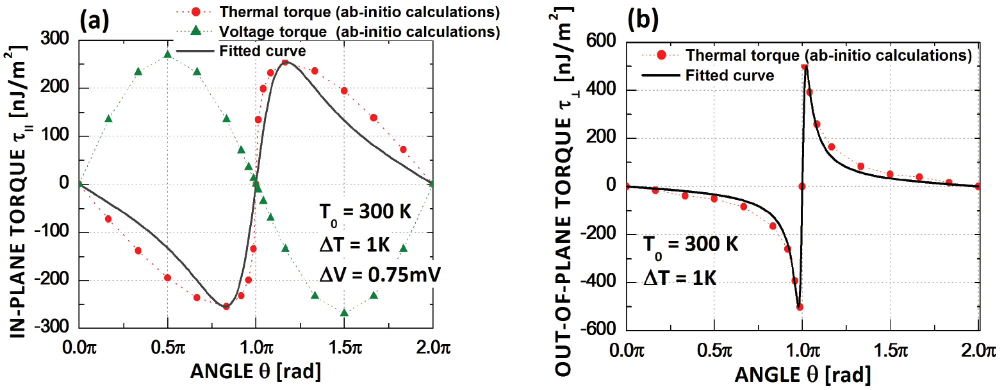

FIG. 2. (Color online) Angular dependence of the (a) in-plane and (b) out-of-plane torques induced by a temperature gradient $\Delta T = 1\,\mathrm{K}$ applied over the MTJ under open-circuit conditions. The average temperature of the junction is $T_0 = 300\,\mathrm{K}$. The barrier consists of three monolayers of MgO, corresponding to a thickness of 0.6 nm. Panel (a) shows, for comparison, a plot of the in-plane torques induced by an electric bias of 0.75 mV computed by first principles (Ref. 33). The MgO thickness and other parameters are the same.

current that represents the nonlocal exchange coupling through the tunnel junction. The thermally induced torque vector acting on the ith layer of free layer is defined by

$$\vec{T}_i = \vec{J}_{i,i-1} - \vec{J}_{i+1,i}. \tag{5}$$

The total thermal torque vector within the free layer is given by $\vec{\tau} = \sum_{i=0}^{N} \vec{T}_i$, where the sum is over all atomic planes in the free layer. In the model calculations, we focus on the thinnest MgO barrier that can be grown coherently in real structures, i.e., three atomic layers of MgO ($\sim$0.6 nm of thickness). According to the *ab initio* calculations, the angular dependence of both thermal torque components is highly skewed; i.e., they deviate from the sine dependence expected for thick tunnel junctions. In Fig. 2, we can see these dependencies for both components of the torque $\vec{\tau}$ for $T_0 = 300\,\mathrm{K}$ and $\Delta T = 1\,\mathrm{K}$. We assume here that the amplitudes $\tau_{\|,\perp}$ from Eq. (3) depend linearly on the temperature gradient ΔT. This assumption agrees well with *ab initio* results for relatively small temperature gradients $\Delta T/T_0 \ll 1$.

In Fig. 2, we also can see that thermal torques have magnitudes comparable to the electrically induced ones. The out-of-plane torque has higher skewness than the in-plane component. Estimated values of skewness coefficients from Eq. (3) are $\Lambda_\| = 3.55$, and $\Lambda_\perp = 29.8$. The first value is relatively high in comparison to the ones in standard metallic spin valves with electrically induced torques.[34] A large Λ implies that thermal torques are larger for the AP than the P configuration, i.e., when the charge current is suppressed.[22] The high STT is related to resonant tunneling through the barrier and multiple scattering between interfacial states that play a similar role as the spin accumulation in metallic spin valves, leading to more efficient spin transfer per transmitted electron. In the P configuration, transmission is relatively high, multiple scattering is suppressed, and the torque is much smaller. In the next sections, we discuss how the torque skewness modifies the dynamical system described by the LLG equation and affects the solutions and critical temperatures for AP → P(P → AP) switching.

IV. CALCULATION OF EQUILIBRIUM POINTS AND THEIR STABILITIES

The calculations presented in this section are based on the method for charge current-induced magnetization dynamics.[35] Here, we introduce new aspects related to the angular torque dependence. In other words, we express the dynamical matrices, as well as their eigenvalues, as a function of

TABLE I. Character of stationary points in terms of the signs of a and b and eigenvalues μ.

a	b	$\mu_{1,2}$	Equilibrium
$-$	$-$	Imaginary	Stable focus
$+$	$-$	Imaginary	Unstable focus
Real	$+$	$\mu_{1,2} < 0$	Stable center
Real	$+$	$\mu_{1,2} > 0$	Unstable center
Real	$+$	$\mu_1 < 0 < \mu_2$	Saddle

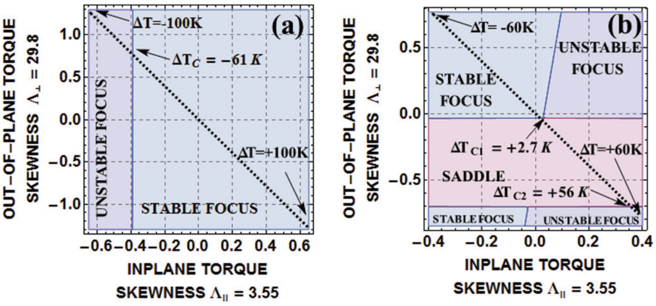

FIG. 3. (Color online) The stability diagram for equilibrium points (a) $\theta = 0$ and (b) $\theta = \pi$. The x and y axes are the in-plane and out-of-plane torque amplitudes $h_\|$ and $h_\perp$, respectively. The black dashed line indicates the thermal torque components with skewness coefficients derived from *ab initio* calculations for Fe|MgO(3ML)|Fe. ΔT is changing from $-100\,\mathrm{K}$ to $+100\,\mathrm{K}$ for $\theta = 0$ and from $-60\,\mathrm{K}$ to $60\,\mathrm{K}$ for $\theta = \pi$. Negative ΔT means that the fixed electrode (polarizer) is cooler than the free one. An increase of ΔT toward negative or positive values corresponds, respectively, to moving from the origin to the top left or bottom right corner of the diagram along the dotted black line.

the $\Lambda_{\parallel,\perp}$ coefficients. Each system, described by a set of differential equations (SDE) in the form $d\vec{x}/dt = f(\vec{x})$, can be characterized by the type and stability of equilibrium points that are defined by setting the right side of the SDE equal to 0, i.e., $f(\vec{x}) = 0$. It is easy to check that for the LLG Eq. (2), two main equilibria exist at the north and south poles: $\theta = 0$ and $\theta = \pi$. These two points correspond to P and AP magnetizations. We can find other equilibria on the unit sphere. The stability of each equilibrium point is parameter dependent. Studying the influence of the parameters on the stability of the equilibria (stability diagrams) provides us initial information about the dynamic behavior of the MTJ without having to carry out full-scale dynamical calculations. In the next subsections, we show how the stability can be determined by linearizing the set of nonlinear differential equations.

A. Linearization and dynamical matrices

The standard linearization procedure begins by finding the points of equilibrium. First, we rewrite LLG Eq. (2) into the matrix form[35]

$$\begin{pmatrix} \dot{\theta} \\ \dot{\phi} \end{pmatrix} = \frac{\Omega_K}{1+\alpha^2} \begin{pmatrix} 1 & \alpha \\ -\frac{\alpha}{\sin\theta} & \frac{1}{\sin\theta} \end{pmatrix} \begin{pmatrix} v_\theta \\ v_\phi \end{pmatrix} = \frac{\Omega_K}{1+\alpha^2} \hat{A} \cdot \hat{v} \tag{6}$$

where

$$\hat{v} = \begin{pmatrix} v_\theta \\ v_\phi \end{pmatrix} = \begin{pmatrix} -\frac{h_\parallel \sin\theta}{\Lambda_\parallel \cos^2\frac{\theta}{2} + \frac{1}{\Lambda_\parallel}\sin^2\frac{\theta}{2}} - h_p \sin\phi \cos\phi \, \sin\theta \\ -\cos\theta \sin\theta - h_p \cos\theta \cos^2\phi \sin\theta + \frac{h_\perp \sin\theta}{\Lambda_\perp \cos^2\frac{\theta}{2} + \frac{1}{\Lambda_\perp}\sin^2\frac{\theta}{2}} \end{pmatrix} \tag{7}$$

Next, we solve the equation for static solutions:

$$\begin{pmatrix} v_\theta \\ v_\phi \end{pmatrix} = \begin{pmatrix} 0 \\ 0 \end{pmatrix} \tag{8}$$

For $\theta = 0$ and $\theta = \pi$, the above equalities hold, so the main equilibria located at the poles of the unit sphere. Direct linearization of the LLG equation around these points is prohibited by the singularity of the spherical surface mapping onto the plane.[35] We follow the method proposed in Ref. 35 that relies on transforming from spherical coordinates into local and nonsingular ones. We express the LLG equation in new coordinates in order to determine the so-called dynamical matrix, which is responsible for the dynamical properties near the poles. First, we linearize the right hand of LLG Eq. (6) around $\theta = 0$:

$$\begin{pmatrix} \dot{\theta} \\ \dot{\phi} \end{pmatrix} = \begin{pmatrix} -\frac{h_\parallel \theta}{\Lambda_\parallel} + \frac{\alpha h_\perp \theta}{\Lambda_\perp} + \theta(-\alpha - \alpha h_P \cos^2\phi - h_P \cos\phi \sin\phi) \\ -1 + \frac{\alpha h_\parallel}{\Lambda_\parallel} + \frac{h_\perp}{\Lambda_\perp} - h_P \cos^2\phi + \alpha h_P \sin\phi \cos\phi \end{pmatrix} \tag{9}$$

At this stage, we can introduce the new nonsingular coordinates[35]

$$\begin{aligned} x &= \theta \sin\phi \\ y &= \theta \cos\phi \end{aligned} \tag{10}$$

with time derivatives

$$\begin{pmatrix} \dot{x} \\ \dot{y} \end{pmatrix} = \begin{pmatrix} \sin\phi & \theta\cos\phi \\ \cos\phi & -\theta\sin\phi \end{pmatrix} \begin{pmatrix} \dot{\theta} \\ \dot{\phi} \end{pmatrix} = J \begin{pmatrix} \dot{\theta} \\ \dot{\phi} \end{pmatrix}. \tag{11}$$

The above equation can be rewritten using the new coordinates into the linearized LLG equation near the $\theta = 0$ point:

$$\begin{pmatrix} \dot{x} \\ \dot{y} \end{pmatrix} = \begin{pmatrix} -\frac{(\Lambda_\perp h_\parallel + \Lambda_\parallel \alpha(\Lambda_\perp - h_\perp))}{\Lambda_\parallel \Lambda_\perp} & -\frac{(-\alpha\Lambda_\perp h_\parallel + \Lambda_\parallel(\Lambda_\perp + \Lambda_\perp h_P - h_\perp))}{\Lambda_\parallel \Lambda_\perp} \\ -\frac{(\alpha\Lambda_\perp h_\parallel + \Lambda_\parallel(h_\perp - \Lambda_\perp))}{\Lambda_\parallel \Lambda_\perp} & -\frac{(\Lambda_\perp h_\parallel + \Lambda_\parallel \alpha(\Lambda_\perp + \Lambda_\perp h_P - h_\perp))}{\Lambda_\parallel \Lambda_\perp} \end{pmatrix} \begin{pmatrix} \theta\sin\phi \\ \theta\cos\phi \end{pmatrix}. \tag{12}$$

$\hat{D}_0$ in

$$\begin{pmatrix} \dot{x} \\ \dot{y} \end{pmatrix} = \hat{D}_0 \begin{pmatrix} x \\ y \end{pmatrix} \tag{13}$$

is the dynamical matrix near the north pole. Near the $\theta = \pi$ point,

$$\begin{pmatrix} \dot{\theta} \\ \dot{\phi} \end{pmatrix} = \begin{pmatrix} \Lambda_\parallel h_\parallel \delta\theta + \alpha(-\Lambda_\perp h_\perp \delta\theta - \delta\theta - h_P \delta\theta \cos^2\phi) + h_P \delta\theta \sin\phi \cos\phi \\ 1 + \Lambda_\perp h_\perp + h_P \cos^2\phi + \alpha(\Lambda_\parallel h_\parallel + h_P \cos\phi \sin\phi) \end{pmatrix} \tag{14}$$

where $\delta\theta \equiv \theta - \pi$. With[35]

$$\begin{aligned} x &= -\delta\theta \sin\phi \\ y &= -\delta\theta \cos\phi \end{aligned} \tag{15}$$

and

$$\begin{pmatrix} \dot{x} \\ \dot{y} \end{pmatrix} = \begin{pmatrix} -\sin\phi & -\delta\theta\cos\phi \\ -\cos\phi & \delta\theta\sin\phi \end{pmatrix} \begin{pmatrix} \dot{\theta} \\ \dot{\phi} \end{pmatrix} \tag{16}$$

the linearized LLG equation at the $\theta = \pi$ point reads

$$\begin{pmatrix} \dot{x} \\ \dot{y} \end{pmatrix} = \hat{D}_\pi \begin{pmatrix} x \\ y \end{pmatrix}, \tag{17}$$

where the dynamical matrix is now

$$\hat{D}_\pi = \begin{pmatrix} -\alpha + \Lambda_\parallel h_\parallel - \alpha\Lambda_\perp h_\perp & 1 + \Lambda_\parallel h_\parallel \alpha + h_P + \Lambda_\perp h_\perp \\ -(1 + \alpha\Lambda_\parallel h_\parallel + \Lambda_\perp h_\perp) & (\Lambda_\parallel h_\parallel - \alpha(1 + h_P + \Lambda_\perp h_\perp)) \end{pmatrix} \tag{18}$$

For the other equilibria, we do not have to introduce new coordinates, because their linearization is straightforward. However, we have not been able to obtain analytical solutions and therefore resorted to numerics. As before, we start with Eq. (6). Because $\theta \neq 0,\pi$, we can divide it by $\sin\theta$ and rewrite it into

$$\begin{pmatrix} \left\{\Lambda_\parallel \cos^2\frac{\theta}{2} + \frac{1}{\Lambda_\parallel}\sin^2\frac{\theta}{2}\right\}(-h_P\cos\phi\sin\phi) \\ \frac{h_\perp - \cos\theta\left(\Lambda_\perp\cos^2\frac{\theta}{2} + \frac{1}{\Lambda_\perp}\sin^2\frac{\theta}{2}\right)}{h_P\cos\theta\left(\Lambda_\perp\cos^2\frac{\theta}{2} + \frac{1}{\Lambda_\perp}\sin^2\frac{\theta}{2}\right)} \end{pmatrix} = \begin{pmatrix} h_\parallel \\ \cos^2\phi \end{pmatrix}. \tag{19}$$

We can square upper equation and substitute $\cos^2\phi$ and $\sin^2\phi$ by expressions obtained from the lower one. The θ angles of the equilibrium points obey

$$\left\{\frac{h_\perp - \cos\theta B(\theta)}{h_P\cos\theta B(\theta)}\right\}\left[\frac{h_P\cos\theta B(\theta) - h_\perp + \cos\theta B(\theta)}{h_P\cos\theta B(\theta)}\right] A(\theta) = \left(\frac{h_\parallel}{h_P}\right)^2 \tag{20}$$

where

$$A(\theta) \equiv \left\{\Lambda_\parallel \cos^2\frac{\theta}{2} + \frac{1}{\Lambda_\parallel}\sin^2\frac{\theta}{2}\right\}, \quad B(\theta) \equiv \left\{\Lambda_\perp \cos^2\frac{\theta}{2} + \frac{1}{\Lambda_\perp}\sin^2\frac{\theta}{2}\right\}$$

Solving Eq. (20) and the second one in Eq. (19) numerically, we find the equilibrium angles θ and ϕ. In order to determine their stability, we multiply matrices $\hat{A}$ and $\hat{v}$ from Eq. (6), leading to the LLG equation:

$$\begin{pmatrix} \dot{\theta} \\ \dot{\phi} \end{pmatrix} = \frac{\Omega_K}{1+\alpha^2} \begin{pmatrix} V_\theta \\ V_\phi \end{pmatrix} \tag{21}$$

Linearizing Eq. (21):

$$\begin{pmatrix} \dot{\theta} \\ \dot{\phi} \end{pmatrix} = \frac{\Omega_K}{1+\alpha^2} \begin{pmatrix} \frac{\partial V_\theta}{\partial\theta} & \frac{\partial V_\theta}{\partial\phi} \\ \frac{\partial V_\phi}{\partial\theta} & \frac{\partial V_\phi}{\partial\phi} \end{pmatrix} \begin{pmatrix} d\theta \\ d\phi \end{pmatrix} = \frac{\Omega_K}{1+\alpha^2} \hat{D}_3 \begin{pmatrix} d\theta \\ d\phi \end{pmatrix} \tag{22}$$

with dynamical matrix

$$\hat{D}_3 = \begin{pmatrix} \left[\begin{matrix} -\frac{2\Lambda_\parallel h_\parallel \cos\theta}{1+\Lambda_\parallel^2+(\Lambda_\parallel^2-1)\cos\theta} - \frac{2\Lambda_\parallel(\Lambda_\parallel^2-1)h_\parallel\sin^2\theta}{\{1+\Lambda_\parallel^2+(\Lambda_\parallel^2-1)\cos\theta\}^2} \\ +\alpha\Big(-\cos^2\theta + \frac{2\Lambda_\perp h_\perp\cos\theta}{1+\Lambda_\perp^2+(\Lambda_\perp^2-1)\cos\theta} - h_P\cos^2\theta\cos^2\phi \\ +\sin^2\theta + \frac{2\Lambda_\perp(\Lambda_\perp^2-1)h_\perp\sin^2\theta}{\{1+\Lambda_\perp^2+(\Lambda_\perp^2-1)\cos\theta\}^2} + h_P\cos^2\phi\sin^2\theta\Big) \\ -h_P\cos\theta\cos\phi\sin\phi \end{matrix}\right] & [-h_P\sin\theta(\cos 2\phi - \alpha\cos\theta\sin 2\phi)] \\ \left[\begin{matrix} \sin\theta\Big(1 - \frac{2\Lambda_\parallel\alpha h_\parallel(1-\Lambda_\parallel^2)}{\{1+\Lambda_\parallel^2+(\Lambda_\parallel^2-1)\cos\theta\}^2} \\ -\frac{2\Lambda_\perp h_\perp(1-\Lambda_\perp^2)}{(1+\Lambda_\perp^2+(\Lambda_\perp^2-1)\cos\theta)^2} + h_P\cos^2\theta\Big) \end{matrix}\right] & [h_P(\alpha\cos 2\phi + \cos\theta\sin 2\phi)] \end{pmatrix} \tag{23}$$

B. Stability of equilibria

In the previous subsection, we derived the dynamical matrices whose eigenvalues identify the nature or the stationary point. We can calculate these quantities by solving the equation

$$\det|\hat{D} - \mu| = 0 \rightarrow \mu^2 - \mu(D_{11} + D_{22}) + (D_{11}D_{22} - D_{12}D_{21}) = 0 \tag{24}$$

Eigenvalues are given by

$$\mu_{1,2} = \frac{(D_{11} + D_{22}) \pm \sqrt{(D_{11} + D_{22})^2 - 4(D_{11}D_{22} - D_{12}D_{21})}}{2} \tag{25}$$

where subscripts indicate components of the dynamic matrix $\hat{D}$. Eigenvalues have the general form

$$\mu_{1,2} = a \pm \sqrt{b} \tag{26}$$

The signs of a and b identify the kind of equilibrium. A short summary can be found in Table I.

We found analytic expressions for the eigenvalues at two main equilibria $\theta = 0$ and $\theta = \pi$. For the north pole ($\theta = 0$), we get

$$\begin{aligned}\mu_{1,2} = -\Bigg\{ & \frac{2\Lambda_\perp h_\parallel + \Lambda_\parallel \alpha(\Lambda_\perp(2+h_p) - 2h_\perp)}{2\Lambda_\parallel\Lambda_\perp} \\ & \pm \frac{\sqrt{-4\alpha^2\Lambda_\perp^2 h_\parallel^2 + 4\alpha\Lambda_\perp h_\parallel(\Lambda_\perp(2+h_p) - 2h_\perp) + \Lambda_\parallel^2\left(\Lambda_\perp^2\left(-4 - 4h_p + \alpha^2 h_p^2\right) + 4\Lambda_\perp(2+h_p)h_\perp - 4h_\perp^2\right)}}{2\Lambda_\parallel\Lambda_\perp}\Bigg\}\end{aligned} \tag{27}$$

and for the south pole ($\theta = \pi$):

$$\begin{aligned}\mu_{1,2} = -\tfrac{1}{2}\big\{ & 2\alpha - 2\Lambda_\parallel h_\parallel + \alpha h_p + 2\alpha\Lambda_\perp h_\perp \\ & \pm\sqrt{-4 - 8\alpha\Lambda_\parallel h_\parallel - 4\alpha^2\Lambda_\parallel^2 h_\parallel^2 - 4h_p - 4\alpha\Lambda_\parallel h_\parallel h_p + \alpha^2 h_p^2 - 8\Lambda_\perp h_\perp - 8\alpha\Lambda_\parallel\Lambda_\perp h_\parallel h_\perp - 4\Lambda_\perp h_p h_\perp - 4\Lambda_\perp^2 h_\perp^2}\big\}\end{aligned} \tag{28}$$

Eigenvalues for the other stationary points have to be calculated numerically. In the next section, we present stabilities of the stationary states and their evolution with respect to the temperature gradient (i.e., thermal torques). We consider two cases: a skewed thermal torque with $\Lambda_\parallel = 3.55$ and $\Lambda_\perp = 29.8$ that represents thin tunnel barriers and a symmetric one ($\Lambda_{\parallel,\perp} = 1$), which corresponds to thicker barriers with seven or more monolayers of MgO.

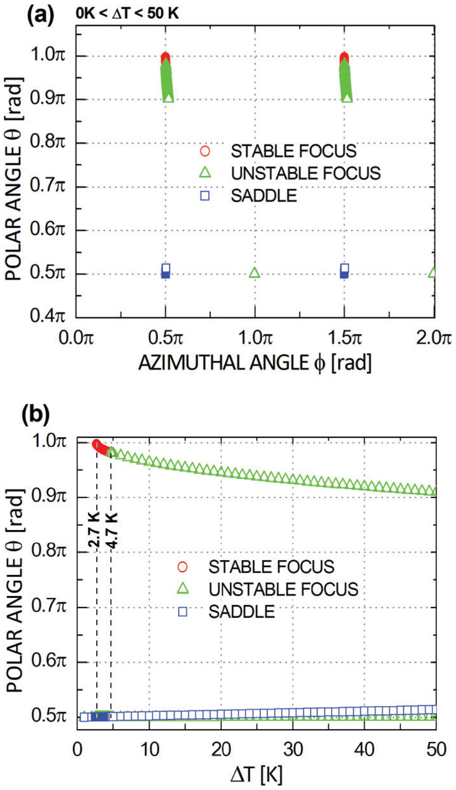

FIG. 4. (Color online) (a) The appearance and movement of nonpolar stationary points when the temperature gradient increase on the (ϕ, θ) plane, and (b) their θ angle position for $\Delta T > 0$. Apart from the two main equilibrium points ($\theta = 0$, π), six other equilibria (grouped in three pairs with period of $\phi = \pi$) have been found: two foci near the south pole ($\theta \approx 3.11$; $\phi \approx \pi/2$, $3/2\pi$), two saddles ($\theta \approx \pi/2$; $\phi \approx \pi/2$, $3/2\pi$), and two foci located at $\theta \approx \pi/2$; $\phi \approx \pi$, 2π.

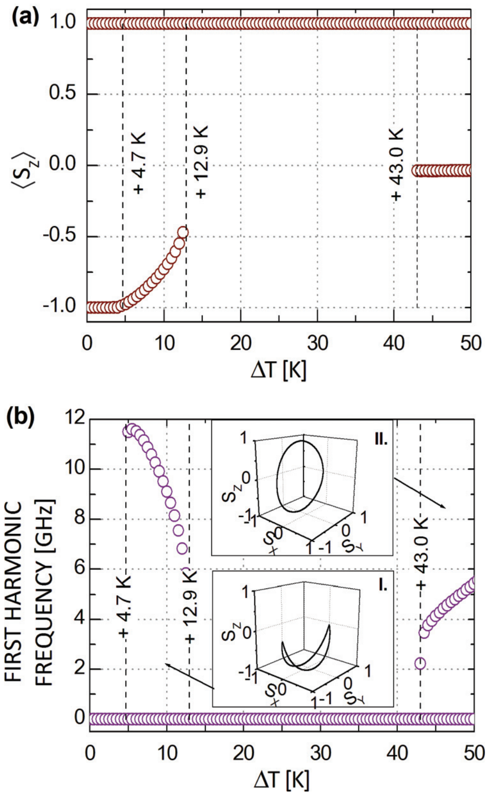

FIG. 5. (Color online) (a) The time average of the S_z component and (b) the first harmonic frequency with respect to ΔT. Two types of precessional states, in-plane oscillations and out-of-plane oscillations, are presented in the insets I and II, respectively.

V. RESULTS

A. Magnetic parameters of the free electrode

Here we focus on the effects of thermal torques on the free magnetic layer dynamics. As mentioned before, the magnitude of these torques depends on the temperature gradient. However, the dynamics of the free layer also depends on its magnetic properties. We used here one set of magnetic parameters that correspond to the discussed Fe/MgO/Fe tunnel junction. We assumed here that the saturation magnetization is $M_S = 1$ T, uniaxial anisotropy field $\mu_0 H_K = 49.9$ T, dimensionless planar anisotropy $h_p = 20$, damping coefficient $\alpha = 0.01$, and thickness of the free electrode $d_f = 2$ nm. We also assume that the torques are absorbed by the magnetic layers, which is the case when they are thicker than a few monolayers.

B. Method of analysis

While our detailed results are given in the next sections, we present here some general remarks about the method, illustrated by the stability diagrams for the $\theta = 0$, π points in Fig. 3. The axes are the magnitudes of in-plane and out-of-plane thermal torques, while the different types of stability (Table I) can be distinguished by the color of the shading. The location of the other stationary points are indicated on the (θ, ϕ) plane in Fig. 4. We plot also the polar position of these points with respect to the temperature gradient in Fig. 5. More information on the spin dynamics can be gained by computing $\langle S_z \rangle$, i.e., the time average of the z component of the magnetization, defined as

$$\langle S_z \rangle = \frac{1}{t'} \sum_i S_z(t_i) \tag{29}$$

where t' denotes the total simulation time of the dynamical steady state and t_i corresponds to temporal discretization step within t'.[36] Moreover, to cover all possible solutions of the LLG equation, we repeat the calculations of $\langle S_z \rangle$ for different initial conditions θ_0 and ϕ_0 over the whole (θ, ϕ) plane, i.e., $\theta \in (0,\pi), \phi \in (0,2\pi)$. We randomize initial conditions for a uniform probability distribution at least 13 times, which should be sufficient to observe all possible solutions for a given temperature gradient ΔT. We observe that for some ΔT, more than one solution may coexist, which may be interpreted as a dynamical hysteresis. The frequency is another useful characteristic of a dynamical state. We calculate Fourier transforms of the time evolution of the $\langle S_z \rangle$ component, and we plot the first harmonic frequency at least 13 times for each gradient temperature in the same manner as for $\langle S_z \rangle$. For precessional states, the first harmonic has a finite frequency. For static P, AP or canted states containing a constant magnetization component, the first harmonic is at zero frequency.

C. Ultrathin MgO barriers

Figure 3 is the stability diagrams for the $\theta = 0$ and $\theta = \pi$ stationary points. The bold dotted straight lines indicate the magnitude of thermal in-plane and out-of-plane torques from

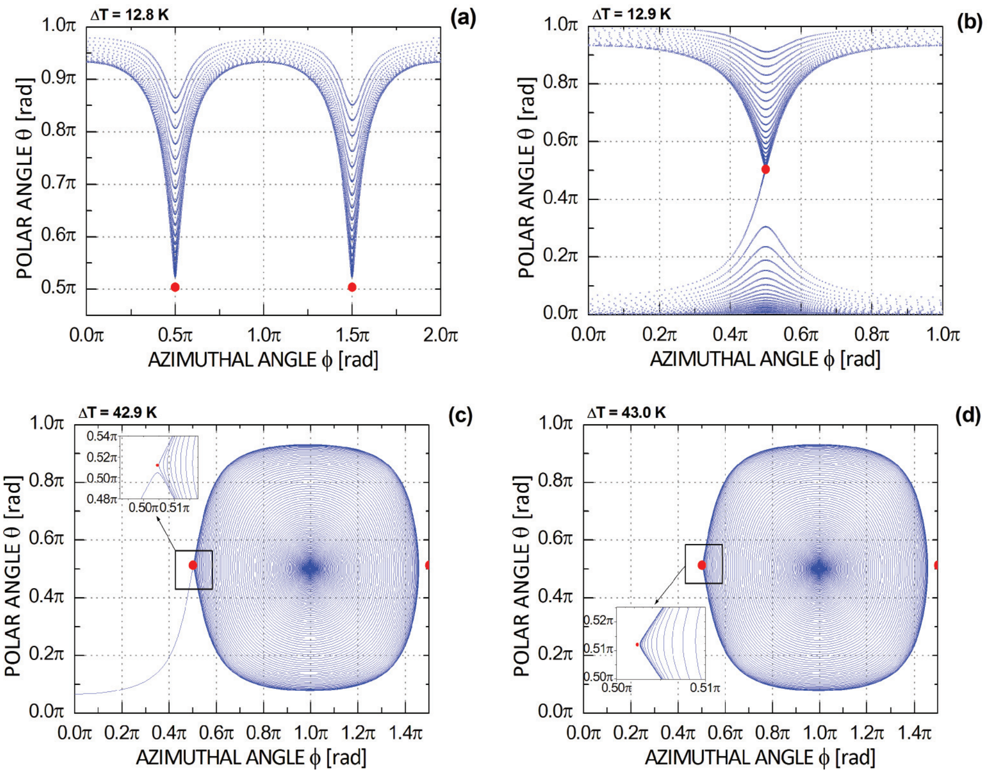

FIG. 6. (Color online) The evolution of the spin-vector trajectory in the (ϕ, θ) (ϕ angle period equals 2π) plane. Red points indicate saddle points. (a) The stable in-plane oscillations are visible. (b) The switching from the AP to the P state is presented. In (c) and (d), the inverse homoclinic bifurcation is shown.

the product of the first-principles results for ultrathin tunnel junctions for the torkance times ΔT. The thermal torques vanish with the temperature gradient $\Delta T = 0$, and $\theta = 0$ and $\theta = \pi$ points are stable foci; i.e., they attract the magnetization vector. Each of these points has its own basin of attraction; i.e., the spin vector may tend toward the 0 point or π point, depending on the point from which we start. In other words, for $\Delta T = 0$, we have two stable solutions. First, let us discuss what is happening when ΔT increases toward positive values. In this case, the north pole [Fig. 3(a)] remains stable even for large temperature gradients. However, at $\Delta T \approx +2.7$ K, the south pole [Fig. 3(b)] changes its stability and becomes a saddle point, which at $\Delta T \approx +56$ K changes its type to an unstable focus, suggesting that for $\Delta T > 0$, the magnetization of the free electrode always favors the P configuration. However, we have to take into account the other stationary points in Fig. 4.

For $\Delta T \approx 2.7$ K, a new equilibrium stationary point appears near $\theta = \pi$ [Fig. 4(b)] that is a stable focus. This means that the stability loss of the south pole is accompanied by the attraction of this new point. Therefore, a near-AP configuration remains stable despite the south pole's instability. This causes an increase in the critical value of ΔT at which the dynamics of the free electrode's magnetization can be induced. The latter appears only at $\Delta T \approx +4.7$ K, where the new focus becomes unstable. That change can be associated with a so-called Hopf bifurcation,[37] which appears when a stable point becomes unstable, creating a limit cycle. In Fig. 5(a), we can see the time-averaged $\langle S_z \rangle$ calculated as described in Sec. V B. The computed first harmonic frequency of the steady dynamical state is shown in [Fig. 5(b)]. At $\Delta T \approx +4.7$ K, $\langle S_z \rangle$ deviates from -1 and increases while ΔT is growing to $+12.9$ K. At the same time, the first harmonic may have nonzero value; i.e., for $+4.7\,\mathrm{K} < \Delta T < +12.9\,\mathrm{K}$, a precessional state appears. There are still two solutions: one is the P state, and the other is a precessional state. The latter state oscillates in plane around an unstable focus located near π [see the insets in Fig. 5(b)].

Above a temperature gradient equal to $+12.9$ K, we do not observe in Fig. 4(b) any change in stability of equilibria points. However, we can see in Fig. 5 that for $+12.9\,\mathrm{K} < \Delta T < +43\,\mathrm{K}$, there is only one stable solution—the P state. In this range of ΔT, we can talk about thermally induced switching from the AP to the P state. Let us now answer the question: what is happening as ΔT is near $+12.9$ K? In Figs. 6(a) and 6(b), we find that answer. At gradient temperature $\Delta T \approx +12.9$ K, the stable limit cycle (precessional state) collides with a saddle point, which suppresses stable precessions. Such behavior is an example of a homoclinic bifurcation[37] reported previously for metallic spin valves.[38] In this range of ΔT, another limit cycle can be found. It is located around an unstable focus ($\theta \approx \pi/2$; $\phi \approx \pi$, 2π). Our calculations show that for $\Delta T < +43$ K, this limit cycle is unstable. In Figs. 6(c) and 6(d), the inverse homoclinic bifurcation can be observed at $+43$ K. For this temperature gradient, an unstable limit cycle [corresponding to out-of-plane oscillations; see the inset in Fig. 5(b)], disconnects from the saddle point, giving the stable limit cycle this time. Above $+43$ K, we have also two stable solutions: P state and out-of-plane oscillations. The change of the π-point character at $\Delta T \approx +56$ K, visible in Fig. 3(b), does not affect the dynamical behavior. This point was an unstable saddle and remains an unstable focus.

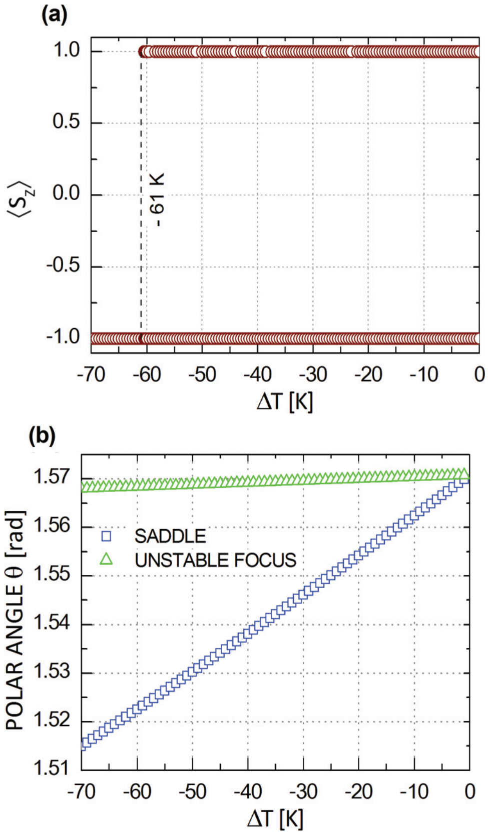

FIG. 7. (Color online) (a) Multiple mean of $\langle S_z \rangle$ component and (b) polar position of the other equilibria (saddle and unstable focus) for the negative temperature gradients.

Now, we discuss briefly the case of $\Delta T < 0$. From Fig. 3(b), we find that the π point is a stable focus for even large temperature gradients. Contrary to that point, the 0 point changes its stability from a stable to an unstable focus $\sim\Delta T \approx -61$ K [Fig. 3(a)]. We can see $\langle S_z \rangle$ [Fig. 7(a)] and polar position of equilibria [Fig. 7(b)] with respect to negative temperature gradients. This time, only two pairs of nonpolar equilibria are present: two saddles ($\theta \approx \pi/2$; $\phi \approx \pi$, 2π) and two unstable foci ($\theta \approx \pi/2$; $\phi \approx \pi/2$, $3/2\pi$). The dynamics is determined only by the stability of the polar equilibria: $\theta = \pi$ and $\theta = 0$. For $\Delta T > -61$ K, two stable solutions coexist: the P state and the AP state. Above the critical value $\Delta T \approx -61$ K, only one stable solution remains, i.e., the AP state. The change of the north pole's stability does not create a stable limit cycle. Rather, it is an example of a so-called subcritical Hopf bifurcation.[37] The limit cycle around the unstable focus observed earlier for positive gradients (as out-of-plane oscillations) does not occur either. Thus, we observe neither a homoclinic bifurcation nor a collision of a stable limit cycle with a saddle point. We suppose that this limit cycle exists but is unstable even for large negative temperature gradients.

D. Thick MgO barriers

In this subsection, we show what is happening when the angular skewness of the STT is reduced to a trigonometric

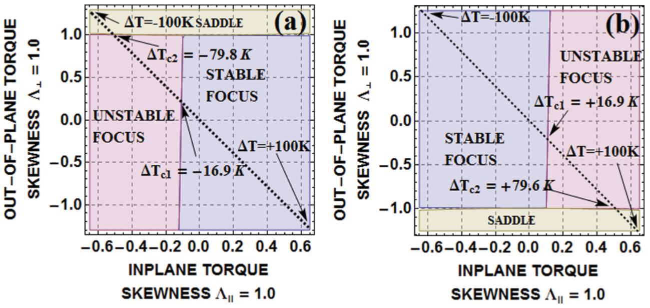

FIG. 8. (Color online) The stability diagrams for stationary points (a) $\theta = 0$ and (b) $\theta = \pi$ for the standard torques in thicker barriers ($\Lambda_\parallel = \Lambda_\perp = 1$).

function for thicker MgO barriers[22] by setting $\Lambda_{\parallel,\perp} = 1.0$ (regular angle dependence). For thicker junctions, the torque amplitudes are much smaller, but for better comparison we fix $\tau^{(0)}_{\parallel(\perp)}$ to the values for the MgO thin barriers. This helps identifying the effects of skewness with possible relevance for device design.

In Fig. 8, the changes in types of polar points can be seen. The 0 point is stable for all positive temperature gradients [Fig. 8(a)]. Similarly, the π point is stable for all negative temperature gradients [Fig. 8(b)]. The stability of the latter changes at $\Delta T_{C1} = +16.9$ K. Then the south pole point is no longer the stable focus but rather changes to the unstable focus. The north pole point loses its stable character (stable focus) at $\Delta T_{C1} = -16.9$ K and becomes unstable focus. Nonpolar points are depicted in Fig. 9. The two types of nonpolar stationary states can be found at angle $\theta \approx \pi/2$. These points are the saddle point and unstable focus. They do not change their stabilities with increasing ΔT toward positive or negative values [Figs. 9(b) and 9(d)]. In contrast to the thin barrier limit, the position of the saddle point changes significantly with ΔT. If we look at the plots of $\langle S_z \rangle$ in Fig. 9(a), we can see that for $\Delta T < 16.9$ K, two solutions are stable P and AP states. At 16.9 K $\langle S_z \rangle$ deviates from -1, what means that π point has lost its stable character. This is Hopf bifurcation of this point. It provides the appearance of a stable limit cycle around the π point. Evidence of that limit cycle (corresponding to in-plane precessions) is nonzero values of the first harmonic frequency [see the inset in Fig. 9(a)]. This periodic solution and the P state are two stable state in that range of ΔT. However, the in-plane oscillations disappear at $\Delta T \approx +19.1$ K. Then the limit cycle collides with the saddle point, losing its stable character. This is homoclinic bifurcation, as already known from the case described in Sec. V C [Figs. 10(a) and 10(b)].

For regular thermal torques, the range of ΔT where the in-plane oscillations are present is very narrow. It is connected to the significant replacement of the saddle point, which moves toward the π point [see Fig. 9(b)]. This is the reason homoclinic bifurcation occurs for smaller amplitudes of the in-plane oscillations in the regular case than in the skew one. For $\Delta T > 19.1$ K, the only stable solution of the LLG equation is the P state. For negative temperature gradients ($-16.9\text{ K} < \Delta T < 0$ K), we find two stable solutions: the AP and P states [see Fig. 9(c)]. At $\Delta T \approx -16.9$ K, the 0 point is no longer stable. It becomes the unstable focus. Contrary to the skew case, for negative ΔT, we recognize supercritical Hopf bifurcation with a stable limit cycle. For $\Delta T < -19.1$ K, only the AP state is stable.

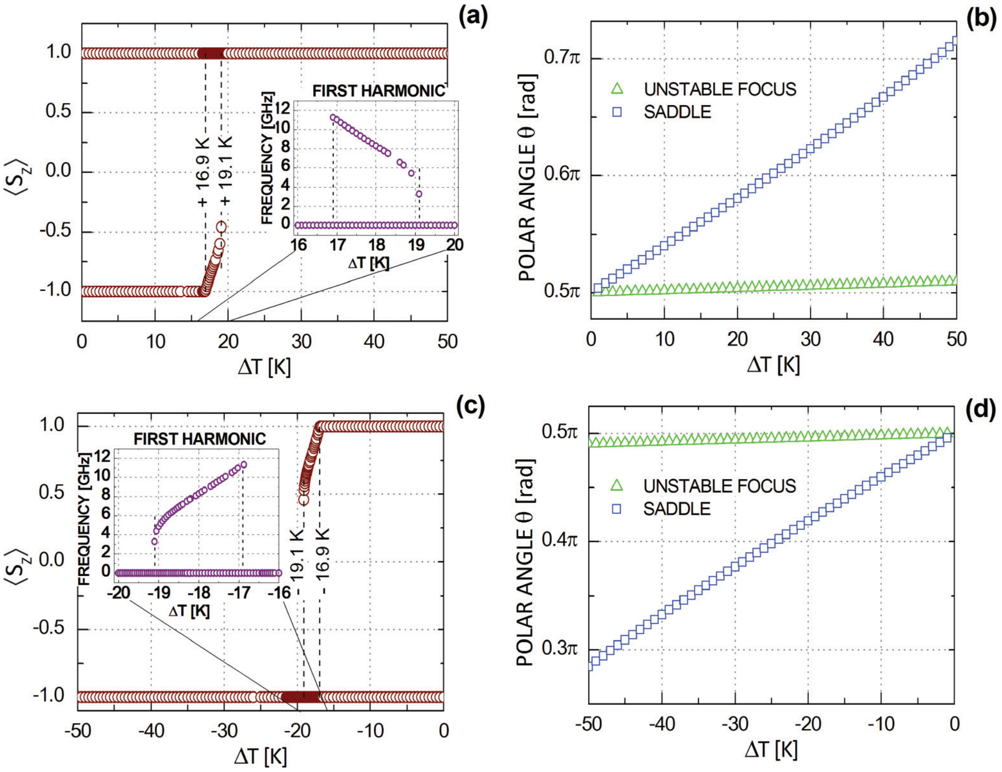

FIG. 9. (Color online) Multiple $\langle S_z \rangle$ components and replacement of the nonpolar equilibria for (a) and (b) positive and (c) and (d) negative temperature gradients for regular thermal torques. Insets: First harmonic frequency dependence on ΔT.

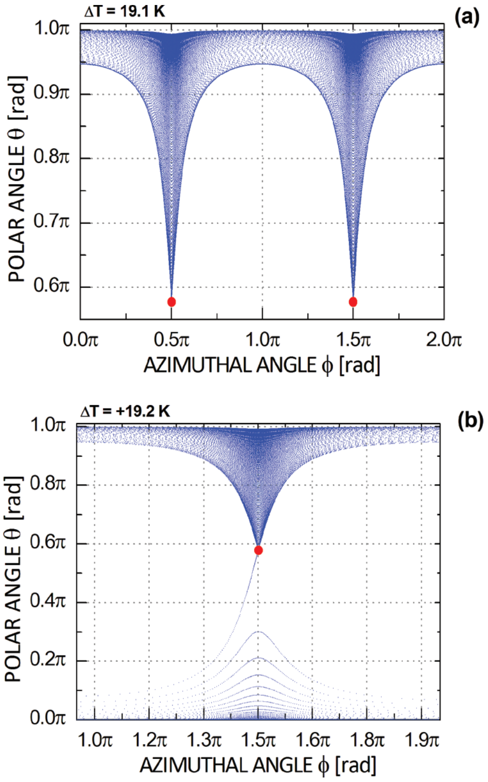

FIG. 10. (Color online) (a) and (b) Homoclinic bifurcation for regular thermal torques. Blue lines indicate the free electrode magnetization's motion on the ϕ-θ plane. Red points are the positions of the saddle points.

VI. SUMMARY

We found that the strong skewness of the angular dependence of thermal torques in ultrathin MTJs modifies their dynamics. We found bifurcations occurring under a temperature gradient. The out-of-plane oscillations exist for skew torques only. Next, the skewness excites in-plane oscillations at a much smaller ΔT than do the regular ones. Furthermore, the range of ΔT for which these in-plane oscillations are present is much narrower for regular compared with skew torques. This is caused by pinning of the saddle point in the latter case and an easier replacement of that point in the former case. Next, the switching from the AP to the P state occurs for smaller ΔT for skewed torques, but from the P to AP state a regular torque is more efficient. Finally, we conclude that the critical ΔT in ultrathin junctions is not governed only by stability of the 0 and π points. Instead, other stationary points may emerge and "delay" the ΔT for which dynamics (and switching) can be induced. Consequently, a naive comparison of thermal torques with an electrically induced one in order to estimate critical ΔT values may fail. This "delay" is found to be ~2 K (but it can be different for other skewness parameters). Our calculated critical switching temperature differences are collected in Table II.

TABLE II. Critical temperature bias calculated for regular and skew (with parameters from first principles) thermal torques with the same amplitudes. The values in parentheses hold for negative ΔT.

Behavior	Critical ΔT (skew case)	Critical ΔT (regular case)
In-plane oscillations inducing	+4.7 K (not observed)	+16.9 K (−16.9 K)
AP to P switching	+12.9 K	+19.1 K
Out-of-plane oscillations inducing	+43 K (not observed)	not observed (not observed)
P to AP switching	−61 K	−19.1 K

We conclude that skew thermal torques may introduce device design problems with thermally driven switching by the much larger ΔT needed to switch from the P to AP state than from the P to AP state. Thicker junctions with symmetric thermal torques are more useful in principle than the thinner ones with very skew torque ones. However, in contrast to the results in Table II, thicker junctions have much smaller absolute torkances with critical temperature differences that are likely to be too large to be practical.

ACKNOWLEDGMENTS

This work has been partially supported by the European Union in the framework of European Social Fund through the Warsaw University of Technology Development Programme realized by the Center for Advanced Studies. It was also supported by Swiss Contribution NANOSPIN grant No. PSPB-045/2010, the FOM Foundation, Marie Curie ITN Spinicur, Reimei program of the Japan Atomic Energy Agency, EU-ICT-7 "MACALO", the ICC-IMR, DFG Priority Programme 1538 "Spin-Caloric Transport". K.X. acknowledges financial support from the National Science Foundation of China (No. 11174037). P.O. acknowledges the hospitality at the Delft University of Technology.

---

[1] J. Slonczewski, Phys. Rev. B **39**, 6995 (1989).
[2] J. Slonczewski, J. Magn. Magn. Mater. **159**, L1 (1996).
[3] L. Berger, Phys. Rev. B **54**, 9353 (1996).
[4] K. Xia, P. J. Kelly, G. E. W. Bauer, A. Brataas, and I. Turek, Phys. Rev. B **65**, 220401 (2002).
[5] I. Theodonis, N. Kioussis, A. Kalitsov, M. Chshiev, and W. H. Butler, Phys. Rev. Lett. **97**, 237205 (2006).
[6] C. Heiliger and M. D. Stiles, Phys. Rev. Lett. **100**, 186805 (2008).
[7] J. C. Sankey, Y.-T. Cui, J. Z. Sun, J. C. Slonczewski, R. A. Buhrman, and D. C. Ralph, Nat. Phys. **4**, 67 (2008).
[8] C. Wang, Y.-T. Cui, J. A. Katine, R. A. Buhrman, and D. C. Ralph, Nat. Phys. **7**, 496 (2011).
[9] P. P. Horley, V. R. Vieira, P. M. Gorley, V. K. Dugaev, J. Berakdar, and J. Barnaś, Phys. Rev. B **78**, 054417 (2008).
[10] J.-G. Zhu, N. Kim, Y. Zhou, Y. Zheng, J. Chang, K. Ju, X. Zhu, and R. M. White, IEEE Trans. Magn. **40**, 2323 (2004).
[11] P. Ogrodnik, M. Wilczyński, J. Barnaś, and R. Świrkowicz, Phys. Rev. B **82**, 134412 (2010).
[12] W. Skowroński, T. Stobiecki, J. Wrona, G. Reiss, and S. Van Dijken, Appl. Phys. Express **5**, 063005 (2012).

[13] O. Boulle, V. Cros, J. Grollier, L. G. Pereira, C. Deranlot, F. Petroff, G. Faini, J. Barnaś, and A. Fert, Nat. Phys. **3**, 492 (2007).

[14] M. Gmitra and J. Barnaś, Phys. Rev. Lett. **96**, 207205 (2006).

[15] P. Baláz, M. Gmitra, and J. Barnaś, Phys. Rev. B **80**, 174404 (2009).

[16] T. Moriyama, G. Finocchio, M. Carpentieri, B. Azzerboni, D. C. Ralph, and R. A. Buhrman, Phys. Rev. B **86**, 060411 (2012).

[17] D. Houssameddine, U. Ebels, B. Delaët, B. Rodmacq, I. Firastrau, F. Ponthenier, M. Brunet, C. Thirion, J.-P. Michel, L. Prejbeanu-Buda, M.-C. Cyrille, O. Redon, and B. Dieny, Nat. Mater. **6**, 447 (2007).

[18] S. I. Kiselev, J. C. Sankey, I. N. Krivorotov, N. C. Emley, R. J. Schoelkopf, R. A. Buhrman, and D. C. Ralph, Nature **425**, 380 (2003).

[19] M. Hatami, G. E. W. Bauer, Q. Zhang, and P. J. Kelly, Phys. Rev. Lett. **99**, 066603 (2007).

[20] J. C. Slonczewski, Phys. Rev. B **82**, 054403 (2010).

[21] K. Uchida, J. Xiao, H. Adachi, J. Ohe, S. Takahashi, J. Ieda, T. Ota, Y. Kajiwara, H. Umezawa, H. Kawai, G. E. W. Bauer, S. Maekawa, and E. Saitoh, Nat. Mater. **9**, 894 (2010).

[22] X. Jia, K. Xia, and G. E. W. Bauer, Phys. Rev. Lett. **107**, 176603 (2011).

[23] N. Liebing, S. Serrano-Guisan, K. Rott, G. Reiss, J. Langer, B. Ocker, and H. W. Schumacher, Phys. Rev. Lett. **107**, 177201 (2011).

[24] M. Walter, J. Walowski, V. Zbarsky, M. Münzenberg, M. Schäfers, D. Ebke, G. Reiss, A. Thomas, P. Peretzki, M. Seibt, J. S. Moodera, M. Czerner, M. Bachmann, and C. Heiliger, Nat. Mater. **10**, 742 (2011).

[25] J. C. Leutenantsmeyer, M. Walter, V. Zbarsky, M. Münzenberg, R. Gareev, K. Rott, A. Thomas, G. Reiss, P. Peretzki, H. Schuhmann, M. Seibt, M. Czerner, and C. Heiliger, arXiv:1301.2042 (unpublished).

[26] M. H. Kryder, E. C. Gage, T. W. McDaniel, W. A. Challener, R. E. Rottmayer, G. Ju, Y.-T. Hsia, and M. F. Erden, Proc. IEEE **96**, 1810 (2008).

[27] J. Z. Sun, Phys. Rev. B **62**, 570 (2000).

[28] J. Slonczewski, J. Magn. Magn. Mater. **247**, 324 (2002).

[29] J. Xiao, G. E. W. Bauer, and A. Brataas, Phys. Rev. B **77**, 180407 (2008).

[30] Y. Tserkovnyak, A. Brataas, G. E. W. Bauer, and B. I. Halperin, Rev. Mod. Phys. **77**, 1375 (2005).

[31] X. Liu, W. Zhang, M. J. Carter, and G. Xiao, J. Appl. Phys. **110**, 033910 (2011).

[32] T. Yoshino, K. Ando, K. Harii, H. Nakayama, Y. Kajiwara, and E. Saitoh, J. Phys. Conf. Ser. **266**, 012115 (2011).

[33] X. Jia, K. Xia, Y. Ke, and H. Guo, Phys. Rev. B **84**, 014401 (2011).

[34] W. H. Rippard, A. M. Deac, M. R. Pufall, J. M. Shaw, M. W. Keller, S. E. Russek, G. E. W. Bauer, and C. Serpico, Phys. Rev. B **81**, 014426 (2010).

[35] Y. B. Bazaliy, B. A. Jones, and S.-C. Zhang, Phys. Rev. B **69**, 094421 (2004).

[36] P. P. Horley, V. R. Vieira, P. M. Gorley, V. K. Dugaev, and J. Barnaś, Phys. Rev. B **77**, 094427 (2008).

[37] L. Perko, *Differential Equations and Dynamical Systems*, Texts in Applied Mathematics, Vol. 7 (Springer-Verlag, New York, 1991).

[38] M. D. Stiles and J. Miltat, in *Spin Dynamics in Confined Magnetic Structures III*, edited by B. Hillebrands and A. Thiaville (Springer-Verlag, New York, 2006), pp. 225.